Supplementary information for

Intercalating Lithium into Lattice of Silver Nanoparticles boosts Catalytic Hydrogenation of Carbon−Oxygen Bond

Xin-ping Duan[a,b], Tianyi Chen[a], Tianxiang Chen[c], Lele Huang[b], Li Ye[a,d], Benedict T.W. Lo[c], Youzhu Yuan [b*], Shik Chi Edman Tsang[a*]

[a]Wolfson Catalysis Centre, Department of Chemistry, University of Oxford, Oxford OX1 3QR, UK

[b] Department of Chemistry, Xiamen University, Xiamen 361005, China.

[c]Department of Applied Biology and Chemical Technology, Hong Kong Polytechnic University, Hong Kong, China

[d]Department of Chemistry, Fudan University (Jiangwan Campus), Shanghai, China.

[*]Emails: edman.tsang@chem.ox.ac.uk and yzyuan@xmu.edu.cn

Experimental Section

Catalyst preparation

The ordered mesoporous silica support, SBA-15 was synthesized via sol-gel method using P123 ($EO_{20}PO_{70}EO_{20}$) as template and tetraethyl orthosilicate (TEOS) as silica precursor following the well-described procedure reported in literature [36]. The Ag–M/SBA-15 (M represents alkali metal, Li, Na, K, Rb and Cs) catalyst with fixed Ag loading (5 wt.%) was prepared by a sequential impregnation method. A known amount of $AgNO_3$ was dissolved in deionized water assisted with ultrasound. Then SBA-15 was then added to the solution. The mixture was stirred vigorously for 1 h and aged at room temperature for 12 h without light exposure to allow the components to fully immerse and diffuse. The obtained solid was dried at 373 K for 6 h, and then added to different concentrations of alkali metal nitrate ($LiNO_3$, $NaNO_3$, KNO_3 or $RbNO_3$) aqueous solution. The above impregnation process was repeated. The final obtained solid was dried at 373 K for 12 h, calcined at 623 K in air for 4 h and then reduced in a $5\%H_2$–$95\%N_2$ atmosphere at 623 K for 3 h to acquire the final catalyst, which is christened as $5Ag_1$–M_x/SBA-15, where x stands for the atomic ratio of alkali metal and Ag. The monometallic catalyst 5Ag/SBA-15 was prepared by a impregnation method as described above. To evaluate the effect of Li in the 5Ag/SBA-15 catalyst, Li specie was first doped in SBA-15, followed by the similar processes above, including drying and calcination, to generate the Li-doped SBA-15 (indicated as Li-SBA-15) and thereafter, subsequent silver species was loaded to the modified support Li-SBA-15 to obtain $5Ag/Li_{0.05}$-SBA-15 catalyst prior to the reduction in H_2.

Catalyst characterizations

Inductively coupled plasma atomic emission spectrometer (ICP-AES) was measured to determine the Ag and alkali metal ion loadings of the catalysts on a Thermo Elemental IRIS Intrepid II XSP. The sample was treated by aqua regia at 363 K for 1 h, and the resultant solution was heated until it evaporated. The residue was diluted with 5% HCl and filtrated to a 25 mL volumetric flask before ICP-AES measurement.

N_2 adsorption-desorption isotherms was measured at 77 K on a Micromeritics TriStar II 3020

porosimetry analyzer. The samples were degassed at 573 K for 4 h prior to the measurements. The Pore size distributions were calculated from desorption branch according to the Barret–Joyner–Halenda (BJH) method. The specific surface area was calculated according to the Brunauer–Emmett–Teller (BET) method. The total pore volume depended on the absorbed N_2 volume at a relative pressure of approximately 0.99.

Powder X-ray diffraction (XRD) patterns were obtained on a Philips PANAlytical X'pert PRO diffractometer equipped with Cu K_α radiation ((λ= 0.15418 nm) and a graphite monochrometer, operating at 40 kV and 30 mA. The diffraction lines were identified by matching them with reference patterns in the JCPDS database. The Scherrer equation was used to calculate crystallite sizes.

Transmission electron microscopy (TEM), high-resolution TEM (HRTEM), scanning transmission electron microscopy (STEM), and energy dispersive X-ray spectroscopy (EDX) measurements were performed on a Philips Analytical FEI Tecnai 30 electron microscope operated at an acceleration voltage of 300 kV. The catalyst powders were dispersed in ethanol by ultrasonic at room temperature for 30 minutes. The obtained supernatant was then dropped into copper grids.

X-ray photoelectron spectroscopy (XPS) was performed using a JPS-9010MC photoelectron spectrometer equipped with an Al K_α X-ray radiation source (*hv* = 1486.6 eV). A flood gun with variable electron voltage (6-8 eV) was used for charge compensation. Each sample was pretreated in an atmosphere of 5%H_2-95%N_2 at 623 K for 4 h and carefully stored under nitrogen atmosphere before XPS measurement. The raw data were corrected for substrate charging with the binding energy (BE) of the C 1S peak at 284.5 eV. The in situ XPS with etching was carried out using Thermo Scientific Nexsa (12kV cathode biased Al K_α) with a spot size of 400μm at the base pressure < 5 x 10^{-10} mbar. The sputtering gun is the Ar 1keV of raster size 1mm x 1mm area: 15s etching period can take ~ ca. 4 atomic layers from a surface in total.

In situ Fourier-transform infrared (FT-IR) spectra was collected on a Nicolet 6700 spectrometer to determine CO adsorption. Prior to test, the dried catalyst (~40 mg) was compressed into a self-supporting wafer and loaded into the in situ cell. The catalyst was reduced at 623 K under H_2 flow

(50 mL min^{-1}) and then evacuated below 10^{-4} Pa for 30 min at the same temperature to remove surface adsorbed hydrogen species. The catalyst wafer was cooled to 303 K and exposed to high purity CO (50 mL min^{-1}) for 10 min and then evacuated below 10^{-4} Pa for 30 min. The FT-IR were collected with a resolution of 4 cm^{-1} and referenced to background before CO soaking under vacuum at the same temperature.

High-resolution powder X-ray diffraction (HRPXRD) using Mo anode was used to optimise the spatial and angular resolution of the Bragg's reflections. Dynamic measurements were conducted at elevated temperatures at 5 °C min^{-1}. Each powder XRD pattern required 15 min of scanning time for a suitable and reliable signal-to-noise ratio. Fine Ag-^{int}Li/C powder was loaded into a 0.5-mm borosilicate glass capillary. High-resolution PXRD data were obtained from the samples. The patterns were collected in the 2θ range 3-60° with 0.002° data binning. Using the TOPAS software, the diffraction patterns were analysed by Le Bail refinement methods to yield the crystallographic parameters. The starting model was based on the Ag (Fm-3m) model by ICSD database code. The scale factor and lattice parameters were allowed to refine for all the diffraction patterns. The quality of the Le Bail refinements of diffraction data has been assured with a low goodness-of-fit (Gof) factor, a low weighted profile factor (R$_{wp}$).

Electron ptychography: Atomic-resolution STEM imaging was performed at 200 kV using a probe-corrected JEOL ARM200CF microscope. A probe-forming aperture of diameter 30 μm was used to yield a convergence angle of 22.3 mrad. The ptychography dataset was collected using the JEOL 4DCanvas, a direct electron, radiation hard pixelated detector, installed on the JEOL ARM200CF. This camera delivers full frame images of 264×264 pixels at a readout speed of 1,150 frames per second (fps). For these experiments, a convergent beam electron diffraction (CBED) pattern was acquired in 4-fold binning mode (66×264 pixels), which increased the readout speed to 4,000 fps. A total of 512×512 probe positions were recorded for a single dataset, obtained in around 90s. The bright-field (BF) disc was set to cover almost the entire detector area by adjusting the camera length and the dark-field signal was collected by an annular dark-field (ADF) detector. The ADF image and ptychographic data set were acquired simultaneously. Electron ptychography was performed on the data acquired with the JEOL 4D Canvas to obtain an electron phase reconstruction of the Pd^{int}B NP.

The phase was retrieved with an in-house ptychography code using the Wigner distribution deconvolution (WDD) method. Specimens were prepared by dipping holey-carbon film Cu TEM grid into the NPs suspension (ultrasonicate NPs powder in ethanol).

NMR: Under dry nitrogen, the sample was packed into a 3.2 mm ZrO_2 rotor and closed with Kel-F lids. All NMR experiments were performed on 400WB AVANCE III spectrometer at room temperature. ^{7}Li MAS NMR spectra were acquired at resonance frequency of 155.6 MHz, using 15^0 pulse with a recycle delay of 300 s at a MAS speed of 20 kHz. LiCl 1M was used as a standard sample for chemical shift reference of Li.

Catalytic testing

The catalytic reactions for vapor-phase DMO hydrogenation were conducted by using a stainless steel fixed-bed tubular microreactor. In a typical method, 200 mg of as-calcined catalyst precursor (40–60 meshes) was loaded into the center of the reactor, and packed with quartz powders (40–60 meshes) in the top. The catalyst precursor was reduced in a $5\%H_2$–$95\%N_2$ atmosphere at 623 K for 4 h (2 K min^{-1}) before the evaluation of the catalytic performance. The catalyst bed was then cooled to the desired reaction temperature. Pure H_2 and 10 wt.% DMO methanol solution were fed into the reactor at a specified H_2/DMO molar ratio with the system pressure of 3.0 MPa. The outlet stream was collected by an automatic Valco 6-port valve at 30 min intervals. The products were analyzed using an online gas chromatography system (Agilent 7890A) fitted with a KB-Wax capillary column (30 m × 0.45 mm × 0.85 μm) and a flame ionization detector (FID) with a relative standard deviation (RSD) of less than 3%. The products were also collected and confirmed using a 7890GC-5975MS system. To obtain different reaction rates and the initial turnover frequency (TOF), the conversion of DMO was maintained below 25%.
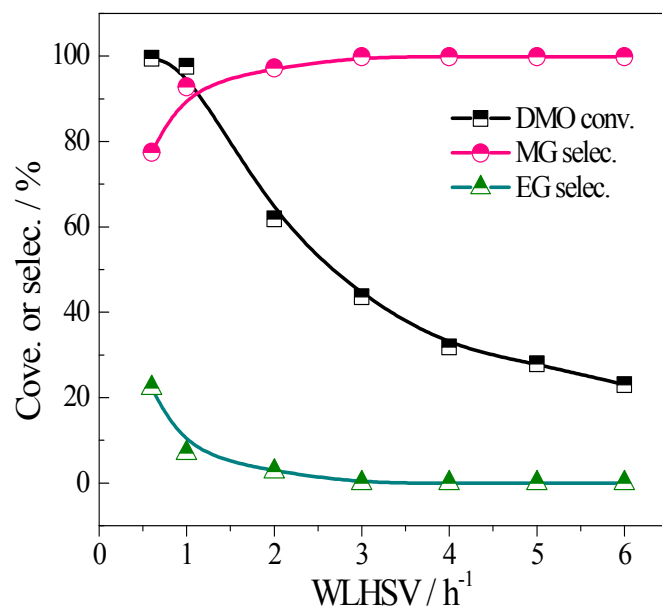
Additional results
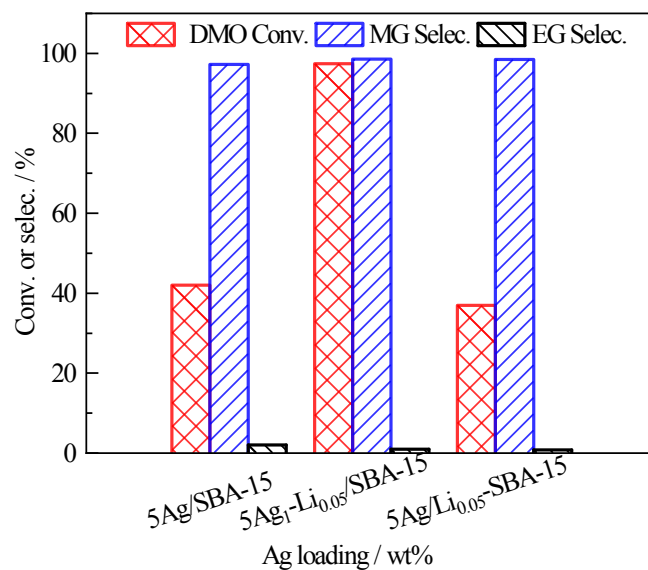
Figure S1 Catalytic performance of different catalysts illustrating the effect of Lithium into silver-based catalysts for DMO hydrogenation to MG.
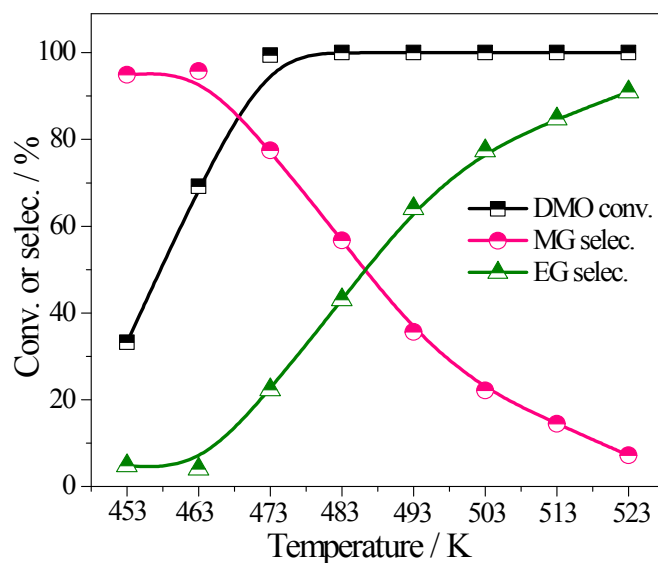
Figure S2 Catalytic performance of $5Ag_1\text{-}Li_{0.05}$/SBA-15 catalysts for DMO hydrogenation at different temperature under reaction conditions of $P(H_2)$ = 3.0 MPa, H_2/DMO = 80, $WLHSV_{DMO}$ = 0.6 h^{-1}.

Figure S3 Catalytic performance of $5Ag_1$-$Li_{0.05}$/SBA-15 catalysts for DMO hydrogenation at different WLHSV under reaction conditions of T = 473 K, $P(H_2)$ = 3.0 MPa, H_2/DMO = 80.
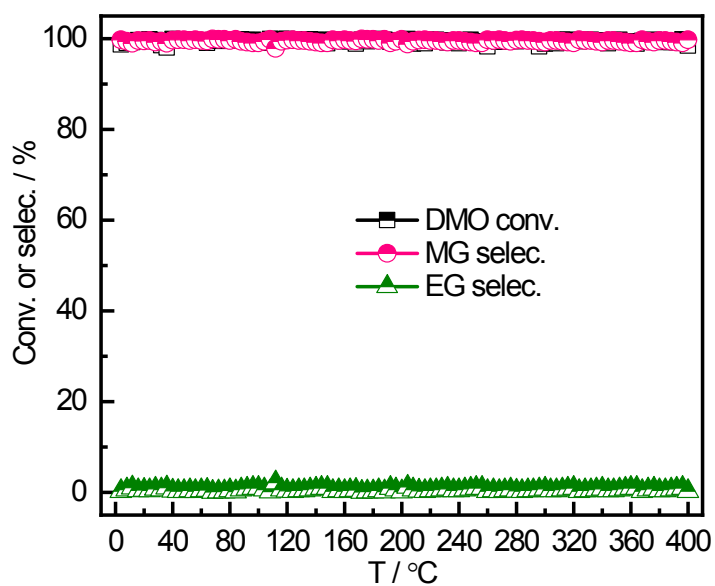
Figure S4 Product distribution of DMO hydrogenation during stability test over $5Ag_1$-$Li_{0.05}$/SBA-15 catalyst.

Size fitting analysis

Table S1 | The list of limiting radius ratio[1-4].

Ag Van der Waals radius[3]	172 pm			
Radius ratio	Coordination arrangement	Structure	Maximum (pm)	minimum (pm)
0.732-0.414	6	octahedral	125.904	71.208
0.414-0.225	4	Tetrahedral	71.208	38.7
Ag metallic radius[4]	144 pm			
Radius ratio	Coordination arrangement	structure	Maximum (pm)	Minimum (pm)
0.732-0.414	6	Octahedral	105.408	59.6
0.414-0.225	4	Tetrahedral	59.616	32.4
Ag ionic radius[5]	129 pm			
Radius ratio	Coordination arrangement	Structure	Maximum (pm)	Minimum (pm)
0.732-0.414	6	Octahedral	94.428	53.406
0.414-0.225	4	Tetrahedral	53.406	29.025
Element	Van der Waals radius	Ion radius* (pm)	Metallic radius (pm)	
Li	182 pm	76 pm	152 pm	
Na	227 pm	102 pm	186 pm	
K	275 pm	138 pm	227 pm	
Rb	303 pm	152 pm[6]	248 pm	

* The ion radius is depedent on the coordination number. Hereins, the ion radius corresponding to CN = 6 is listed.

EELS of the Ag-^{int}Li/C NPs

EELS data were acquired in STEM on a JEOL ARM-200F operating at 80 kV equipped with a Gatan GIF Quantum 965 ER spectrometer. The semi-convergence angle was 22.3 mrad. A 5 mm spectrometer entrance aperture was used, which at the 4 cm camera length of the experiments corresponded to a 37.94 mrad acceptance angle.
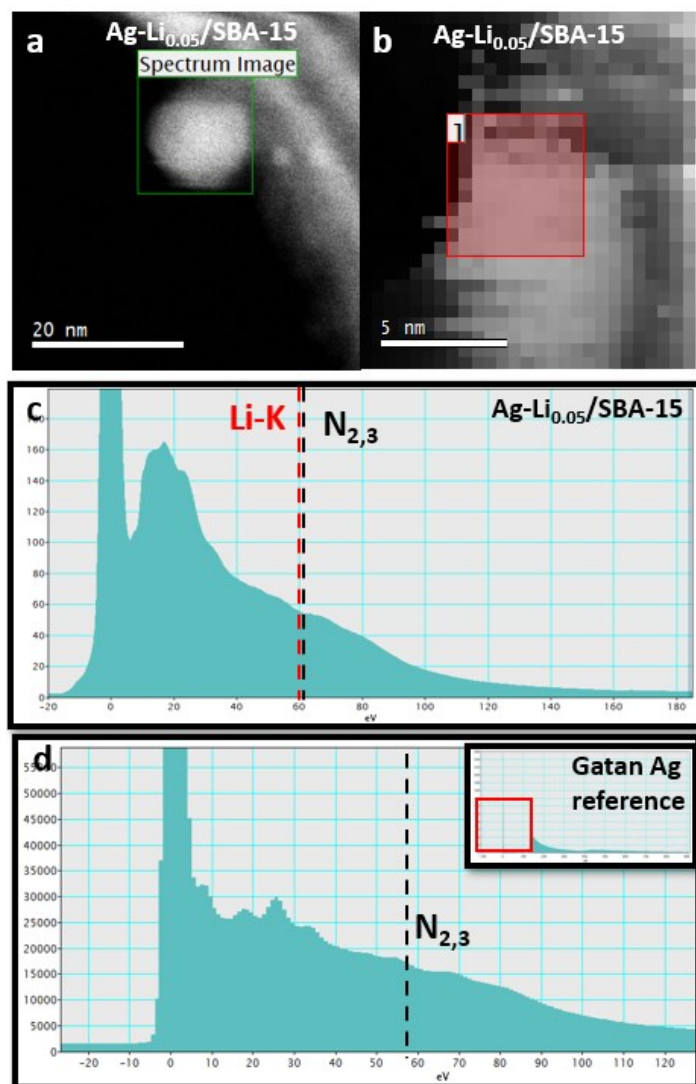
Figure S5. EELS study of Ag-Li$_{0.05}$/SBA-15. a. ADF image of the Ag-Li$_{0.05}$/SBA-15, where EELS spectra were taken along each pixel of the selected area. b. EELS spectra image of a Ag-Li$_{0.05}$ NP hanging above the vacuum. c. EELS spectra of the selected square in EELS in the spectra image. d. Gatan EELS Ag reference spectrum updated on its office website.[5] The location of the Li-K edge and Ag-N$_{2,3}$ edge are annotated with the black and red line, respectively.[6]

ssNMR

To confirm and identify the nature of Li in the samples, ^{7}Li NMR spectra of LiNO₃ before and after reaction with SBA-15 with and without Ag are compared (Fig. S6). There is a typical broad peak located at 0.71 ppm corresponding to the chemical shift of commercial condensed state of LiNO₃. After thermal and reductive treatments of LiNO₃ with SBA-15 at 623K for three hours, a doublet that can be deconvoluted into two peaks locating at 0.91 and -0.49 ppm. According to the literature, the chemical shift of lithium source,[7,8] peaks at -0.91 ppm can be assigned to the isolated Li^+. However, the adjacent more deshielding peak located at -0.49 pm is attributed to the reduced form of Li. It is interesting to note that no such reduced 'Li' when it was placed in the proximity of Ag phase, indicate of the efficient electron transfer may protect the interstitial Li^+ in Ag lattice from its surface reduction.
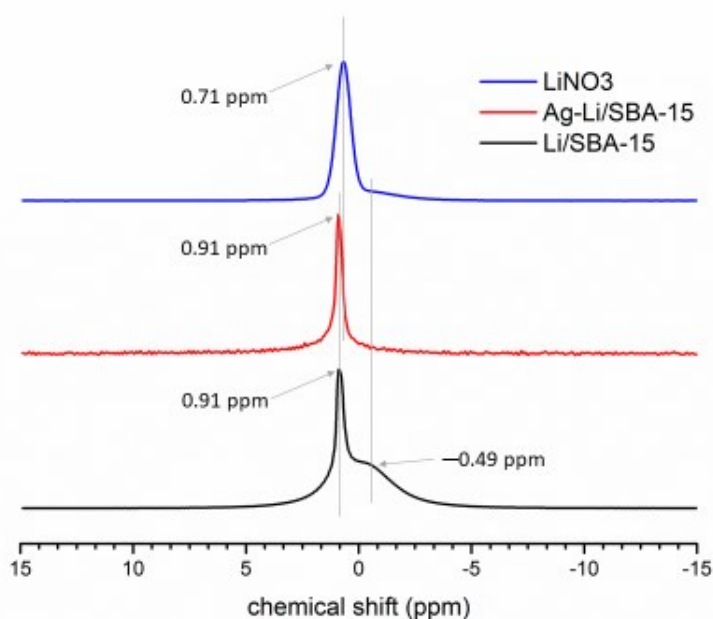
Figure S6. [7]Li MAS spectra of LiNO₃ before and after reactions with SBA-15 with and without Ag are compared: the peak located at 0.71 ppm is attributed to the LiNO₃; reductive treatments of LiNO₃ with SBA-15 at 623K for three hours give a doublet that can be deconvoluted into two peaks at 0.91 and -0.49 ppm, respectively; the same reductive treatments of LiNO₃ with Ag/SBA-15 give no deshielded peak of -0.49 ppm indicative of the electron transfer.
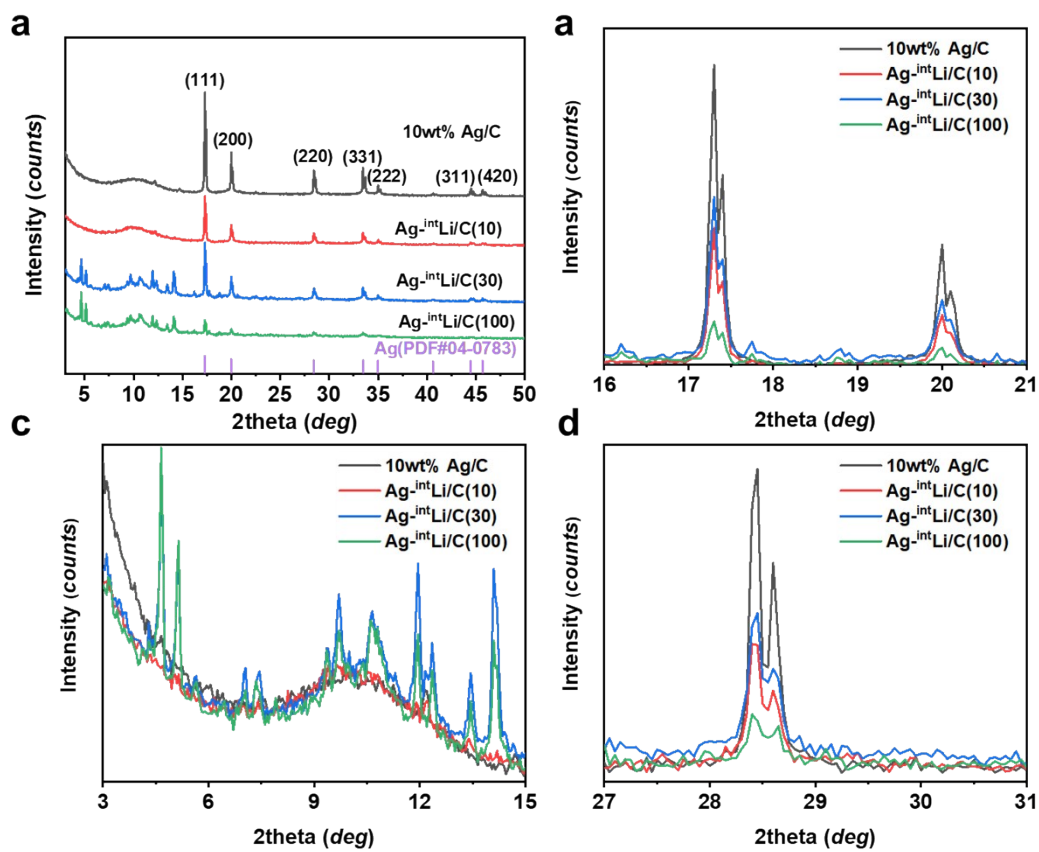
PXRD

Synthesis of model materials for PXRD, PDF and XPS analyses

10 wt % Ag/C synthesis

(0.500 g) 10 wt% Ag/C was prepared by the excessive impregnation method. (0.0774 g) $AgNO_3$ and 0.450 g of active carbon are sonicated in the 100 mL of water for 30 minutes. The $AgNO_3$ solution was stirred and dried at 383 K until evaporating all moisture. The precipitate was then calcinated for 4 hours at 523 K and then reduced at 573 K with a temperature ramping rates of 2 K min^{-1} by 10% H_2/N_2 gas for 4 hours.

10 wt % Ag-^{int}Li/C synthesis

0.1g of 10 wt% Ag/C was mixed with different amount of $Li(OAc).2H_2O$ (100, 30 and 10 molar equivalent, 0.612 g, 0.092 g and 0.031 g, respectively) by mortar and pestle. Grind the mixture until yielding a homogeneous phase. The mixture was heated at N_2 system with ramping rate 10 K min^{-1} up to 473 K for 2 hours.

Figure S7. PXRD pattern measured at 25°C of Ag/C and Ag-^{int}Li/C within different Li/Ag molar ratio (100, 30 and 10), MoKα, λ= 0.7093 Å.

Table S2. Crystallographic data of the XRD measurements of Ag/C and Ag-^{int}Li/C.

	Ag/C	Ag-^{int}Li/C
X-ray energy (keV)	17.5	17.5
Beamline	Rigaku SmartLab SE-3kW	Rigaku SmartLab SE-3kW
Wavelength (Å)	0.7093(1)	0.7093(1)
2θ - zero point (°)	-0.00858(8)	0.00345(1)
Space group	Fm-3m	Fm-3m
Crystal system	Cubic	Cubic
Lattice Parameters (Å)	4.08144(8)	4.08255(3)
2θ range for refinement (°)	15-50	15-50
Detector	1D-Solid-state Detector	1D-Solid-state Detector
Refinement methods	Rietveld	Rietveld
R_{wp}/R_{exp}/R_p (%)	8.479/7.841/6.554	12.800/8.434/10.293
Gof	1.081	1.518

R_{wp}: weighted profile; R_{exp}: expected; R_p: profile; *gof*: goodness-of-fit
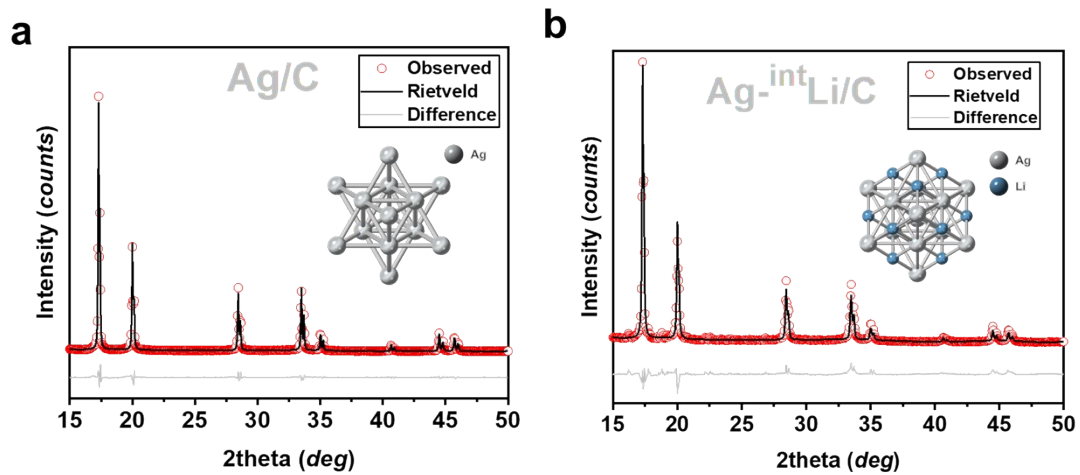
Figure S8. XRD and Rietveld refinement measured at 25 °C. (a) Ag/C and (**b**) Ag-^{int}Li/C. The corresponding Rietveld refined crystal structures are shown in the picture. Atoms are represented in ball/sticks along [111]: Grey = Ag, and Blue= Li.

XPDF

Synthesis of Model material for XPDF analysis

90 wt % Ag/C synthesis

(1.200 g) 90 wt%Ag/C was prepared by the excessive impregnation method. (0.7078 g) $AgNO_3$ and 0.50 g of active carbon are sonicated in the 100 mL of water for 30 minutes. The $AgNO_3$ solution was stirred and dried at 383 K until evaporating all of water. The precipitate was then calcinated for 4 hours at 523 K and then reduced at 573 K with a temperature ramping rates of 2K min^{-1} by 10% H_2/N_2 gas for 4 hours.

90 wt % Li-Ag/C synthesis

0.1g of 90 wt % Ag/C was mixed with 0.07292 g $Li(OAc).2H_2O$ (2 molar equiv) by mortar and pestle. Grind the mixture until yielding a homogeneous phase. The mixture was heated at N_2 system with ramping rate 10 $Kmin^{-1}$ up to 473 K for 2 hours.


PDFgui refinement of finite-size NCs

Rigaku Smartlab diffractometer (3kW, equipped with Mo X-ray anode) was used for the collection of the X-ray total scattering data. The measurements collected scattering signals over the 2θ range of 3-150° using a 0.5-mm borosilicate capillary sample holder. It is capable of measuring a maximum Q-range of 17 $Å^{-1}$. A typical measurement lasts for about 3 hours.

Using Rapid Acquisition Pair Distribution Function method, it is possible to measure the distances between atoms within this sample.[9] For XPDF data treatment, we employed the Rigaku in-built software for the subtraction of air and capillary background. Data optimization was carefully treated through manual operation.

The PDF fitting was performed using PDFgui, where the scale factor, lattice parameters, dampening factor, broadening factor were set to be refined. Also, the fit range is set to be from 1.8 to 9.9 Å, with a Q_{max} of 14.6 $Å^{-1}$. The model atomic configurations of Ag-^{int}Li/C were built based on Li occupying the octahedral sites at (0.5, 0.5, 0.5) based on fundamental crystallography.

Insitu XPS with Sputtering

Li1s Scan
10 Scans, 400µm, Standard, 0.10 eV
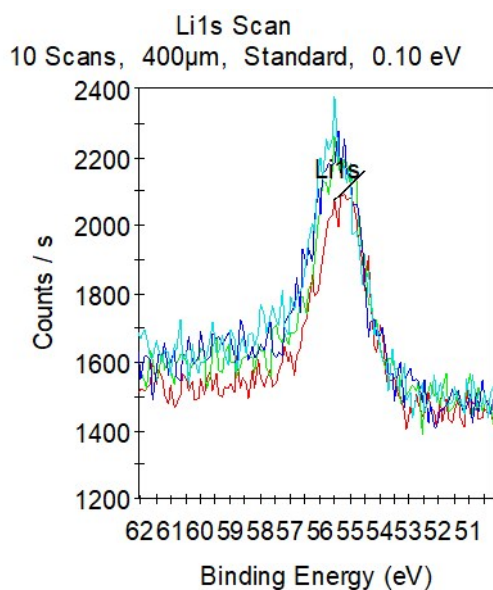
Etch Level (EtchLevel)	O1s	Ag3d	F1s	Si2p	Li1s
	Atomic % (%)	Atomic % (%)	Atomic % (%)	Atomic % (%)	Atomic % (%)
0	12.0386	25.4270	2.29397	1.03852	1.9346
1	10.4267	34.0753	1.30255	0.849684	2.13867
2	9.83579	38.5944	1.18085	0.824637	2.42149
3	9.45185	41.0670	1.02882	0.805863	2.17725

Figure S9. XPS for Li_{1s} with different etching times. Using different etching (sputtering) times cause over model materials of AgLi/C, signals due to surface impurities such F and Si can be dramatically attenuated due to removal of top atomic layers but the Ag/Li ratio maintains indicative of inclusion of Li into the Ag phase

Examples of Crystallographic stacking faults, twinning models

Intrinsic stacking fault: ABCABCABCA $\rightarrow$ ABCACABCA
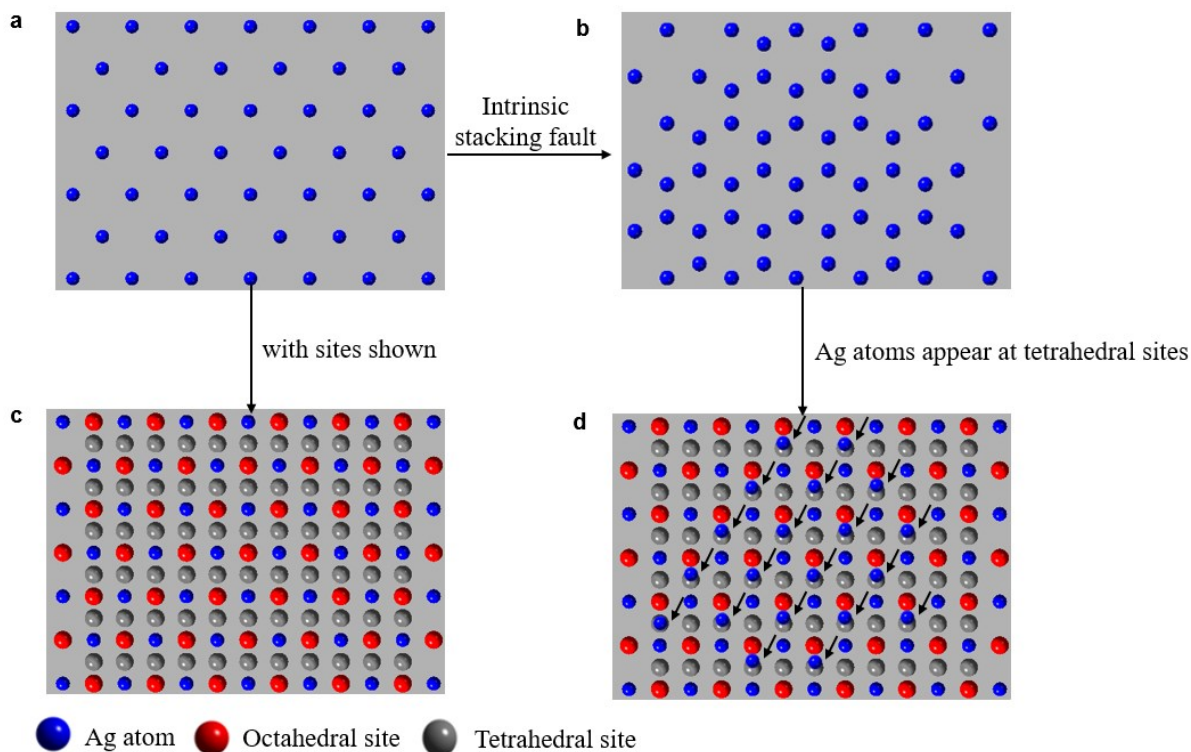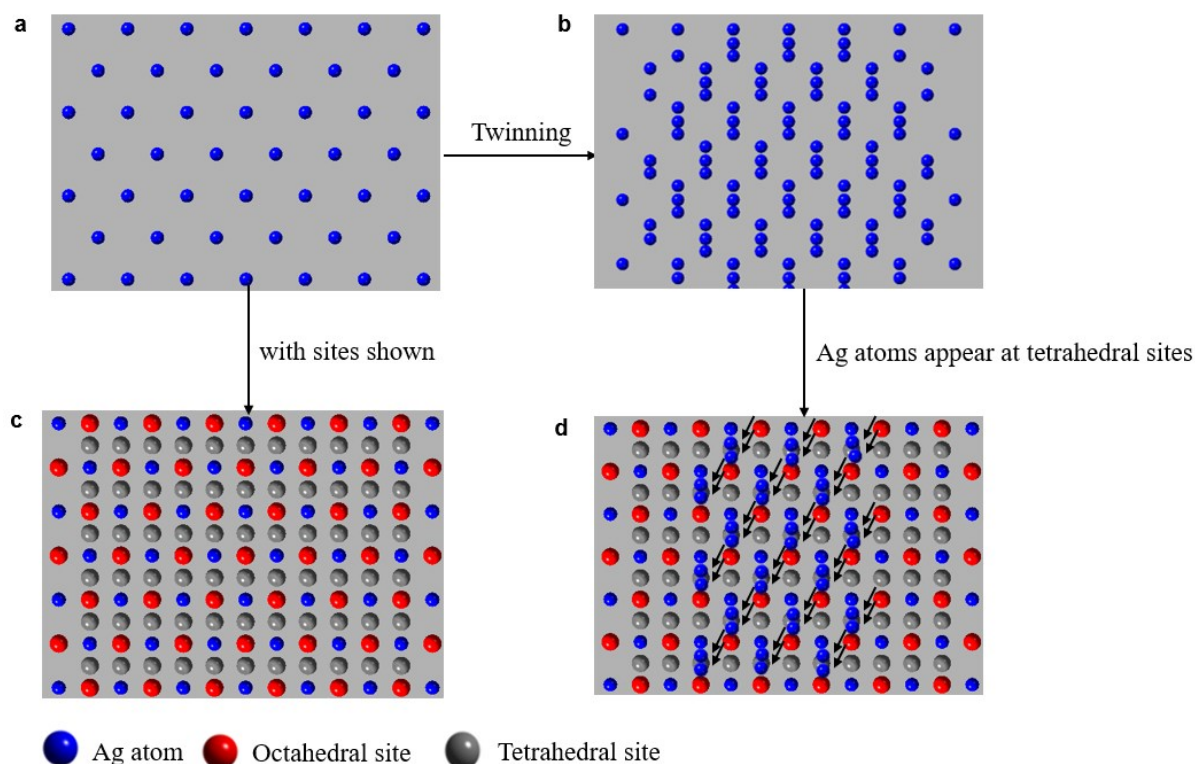

Figure S10. Example of a Ag-^{int}Li/C intrinsic stacking fault model. Blue dots represent Ag atoms; red dots represent octahedral sites; grey dots represent tetrahedral sites. (a) Ag atomic configuration oriented in a <110> direction. (b) demonstrates an example of Ag atomic configuration projected along a [-1 1 0] direction if an intrinsic stacking fault happens. (c) Ag atomic configuration oriented in a <110> with octahedral sites and tetrahedral sites shown. (d) partially demonstrates the positions where Ag atom may emerge if an intrinsic stacking fault happens. These models show no atomic occupancy at the observed octahedral site columns, but rather atomic occupancy appearing close to tetrahedral sites.

Extrinsic stacking fault: ABCABCABCA→ABCACBCABC
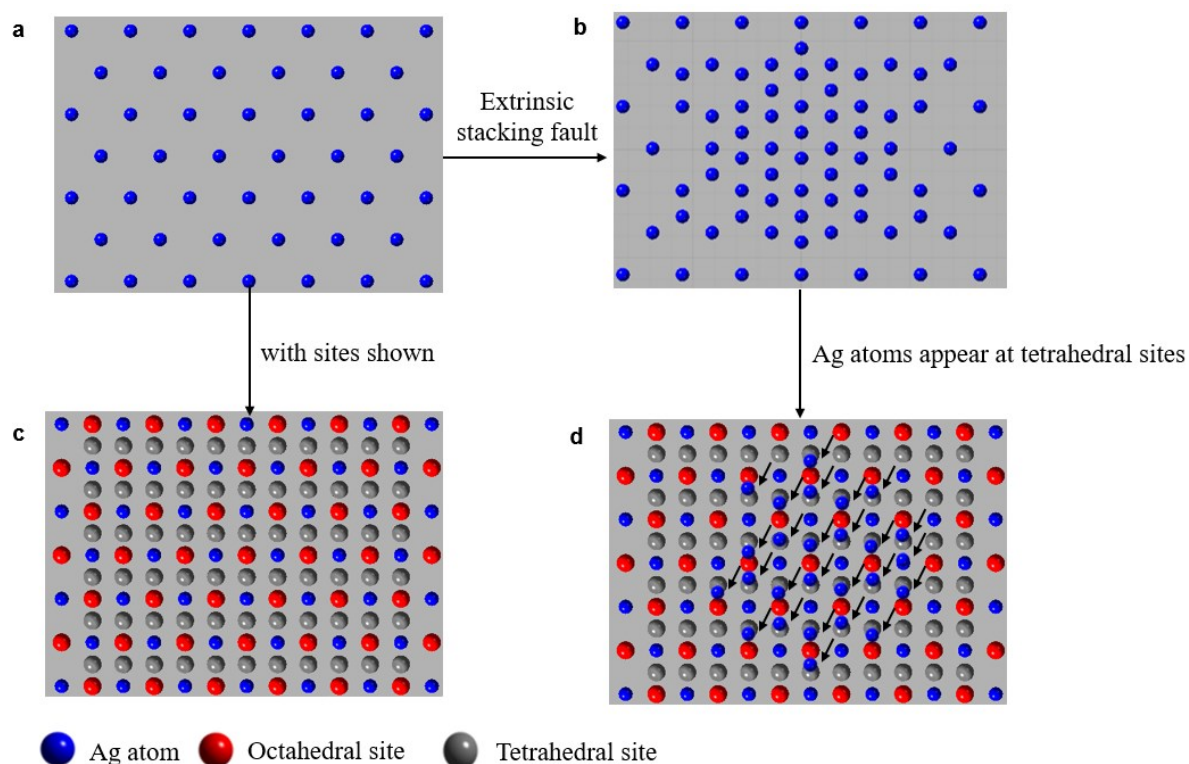
Figure S11. Example of a Ag-^{int}Li/C extrinsic stacking fault model. Blue dots represent Ag atoms; red dots represent octahedral sites; grey dots represent tetrahedral sites. (a) Ag atomic configuration oriented in a <110> direction. (b) demonstrates an example of Ag atomic configuration projected along a [-1 1 0] direction if an extrinsic stacking fault happens. (c) Ag atomic configuration oriented in a <110> with octahedral sites and tetrahedral sites shown. (d) partially demonstrates the positions where Ag atom may emerge if an extrinsic stacking fault happens. These models show no atomic occupancy at the observed octahedral site columns, but rather atomic occupancy appearing close to tetrahedral sites.

Twinning: ABCABCABCA→ABCACBA; twinning plane is A plane

Figure S12. Example of a Ag-^{int}Li/C twinning fault model, where plane A is a twinning line. Blue dots represent Ag atoms; red dots represent octahedral sites; grey dots represent tetrahedral sites. (a) Ag atomic configuration oriented in a <110> direction. (b) demonstrates an example of Ag atomic configuration projected along a [-1 1 0] direction if a twinning fault happens. (c) Ag atomic configuration oriented in a <110> with octahedral sites and tetrahedral sites shown. (d) partially demonstrates the positions where Ag atom may emerge if a twinning fault happens. These models show no atomic occupancy at the observed octahedral site columns, but rather atomic occupancy appearing close to tetrahedral sites.

Twinning: ABCABCABCA→BCABACB; twinning plane is B plane
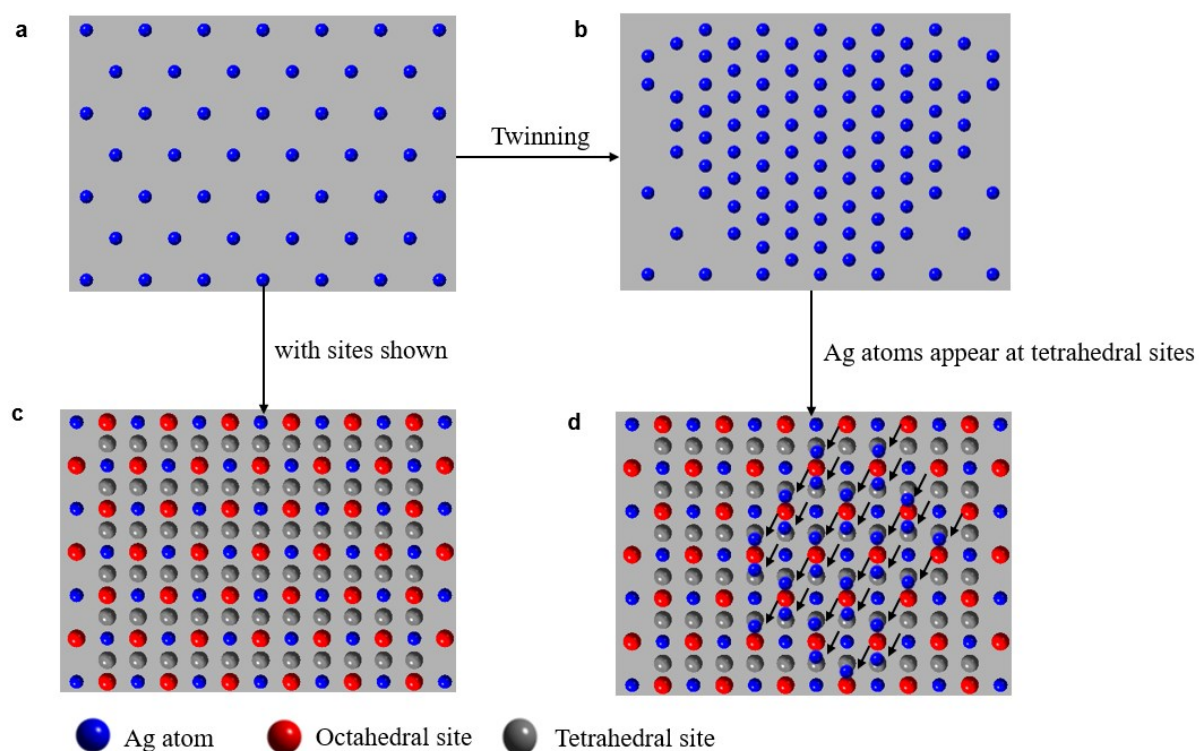
Figure S13. Example of a Ag-^{int}Li/C twinning fault model, where plane Li is a twinning line. Blue dots represent Ag atoms; red dots represent octahedral sites; grey dot represent tetrahedral sites. (a) Ag atomic configuration oriented in a <110> direction. (b) demonstrates an example of Ag atomic configuration projected along a [-1 1 0] direction if a twinning fault happens. (c) Ag atomic configuration oriented in a <110> with octahedral sites and tetrahedral sites shown. (d) partially demonstrates the positions where Ag atom may emerge if a twinning fault happens. These models show no atomic occupancy at the observed octahedral site columns, but rather atomic occupancy appearing close to tetrahedral sites.
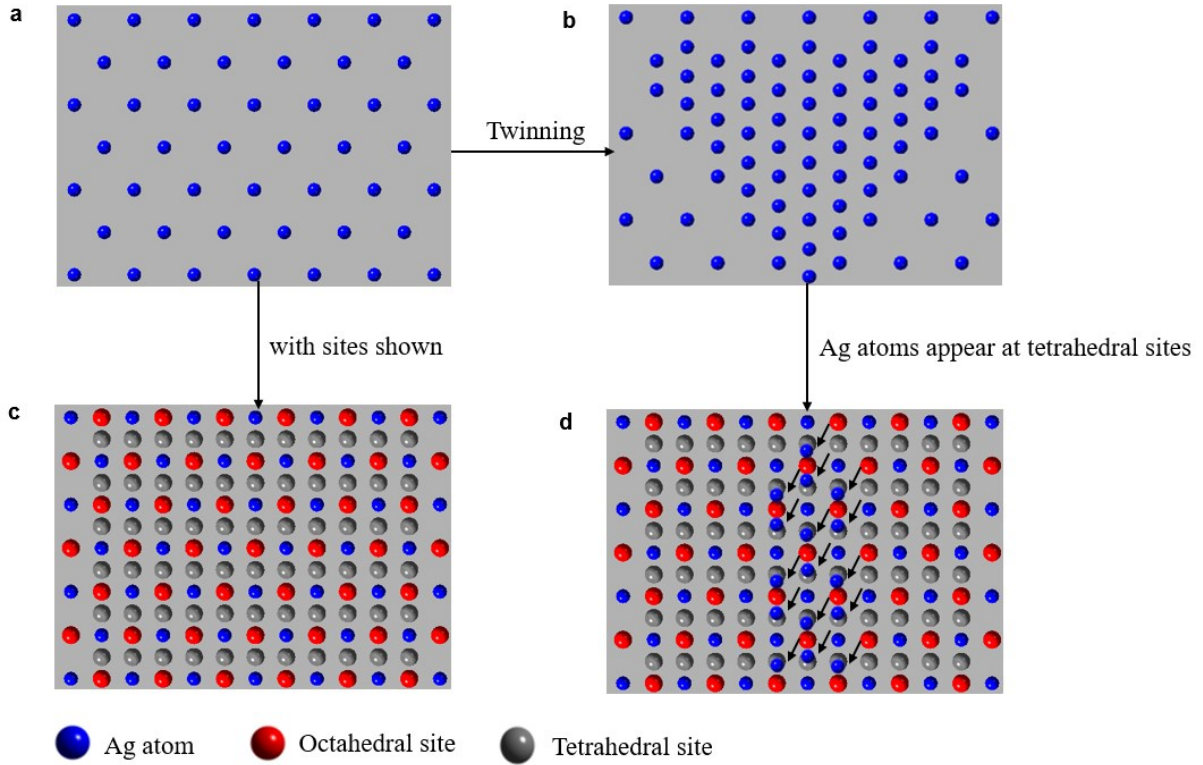
Twinning: ABCABCABCA→CABCBAC; twinning plane is C plane

Figure S14. Example of a Ag-^{int}Li/C twinning fault model, where plane C is a twinning line. Blue dots represent Ag atoms; red dots represent octahedral sites; grey dots represent tetrahedral site. (a) Ag atomic configuration oriented in a <110> direction. (b) demonstrates an example of Ag atomic configuration projected along a [-1 1 0] direction if a twinning fault happens. (c) Ag atomic configuration oriented in a <110> with octahedral sites and tetrahedral sites shown. (d) partially demonstrates the positions where Ag atom may emerge if a twinning fault happens. These models show no atomic occupancy at the observed octahedral site columns, but rather atomic occupancy appearing close to tetrahedral sites.

Ptychographic imaging simulation

Coherent electron diffraction patterns (CBEDs) were calculated using the multislice method[10,11] implemented in the MULTEM software.[12]

For the Ag^{-int}Li/C phase (FCC: *Fm-3m*, *a* = 4.090 Å) a super cell size projected in a [010] plane, of 2.8143 nm x 2.7860 nm was used. The crystal thickness in the beam direction is 2.9 nm, which is the approximately distance between the observation region to the edge. For the scanned region, a numerical real space grid of 60 x 84 scan positions were used with a sampling resolution of 0.14 Å /pixel.

In the calculations, entire thickness was used to slice the potential. Thermal vibrations were included using a frozen phonon approach[13,14] following an Einstein model with 30 phonon configurations. The Debye Waller factors of the elements were calculated, in light of the data reported in reference[11]. The main parameters used in the simulations are summarized in Table S6.

To restore the object wavefunction from the calculated 4D STEM dataset, a Wigner Deconvolution Distribution[15] algorithm was used as indicated in the main manuscript.

Table S6. | Parameters of the multislice calculation.

Accelerating Voltage (kV)	200
Phonon configuration	30
Potential parameterization	Lobato et al.[12]
Slice thickness mode	Whole thickness
Probe convergence semi-angle (mrads)	22.3
Scan grid (reciprocal space)	1024
Scan grid (real space)	60 × 84
Pixel size	0.14, 0.14
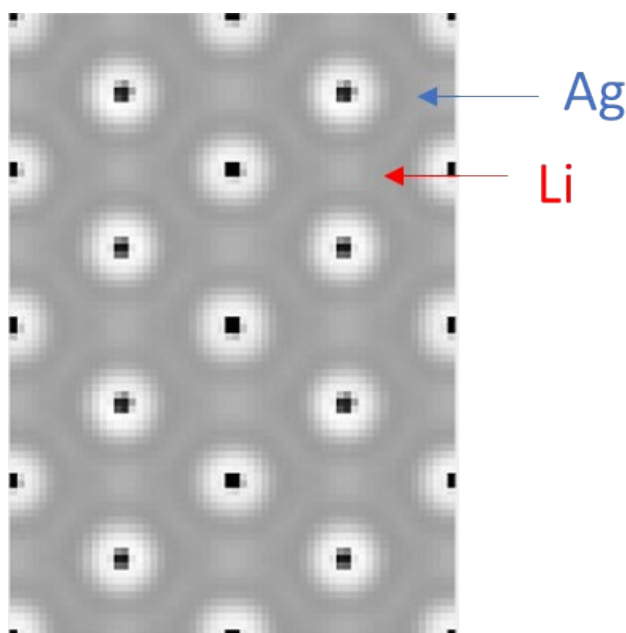
Figure S15. Calculation of the model showing the phase image for a Ag-^{int}Li with a thickness of 2.9 nm. Li atoms can be seen at interstitial sites when if the Li site occupancy is about 100%. Phase contrast reversal and wrapping is evident at Ag atomic columns. This behavior is attributed to dynamical scattering of the electrons, which influence the multiplicative approximation. This phenomenon partially contributes to the well-known contrast mismatch between experimental phase images and simulations, named as the Stobbs factor[16,17], which is a long term challenge in the electron microscopy field.

It should be noted that according to Fig. 6 (b) in the main text, the typical Z-contrast STEM-ADF image of an enlarged area of the NP; Li in octahedral position is hardly visualized. The quality of images was also the same as that of Ag NP without Li. However, ptychographic phase image reconstructed using a Wigner Distribution Deconvolution (WDD) method after aberration correction (see SI) to LiAg shows a weak contrast but visible in octahedron positions (labelled blue in the Fig. 6d) between the Ag columns (labelled white), which can be superimposed to the model predicted by XPDF within the degree of distortion. The simulated image (Fig. S15) shares the same difficulty in the contrast depicting the poor electron scatter of Li compared to Pd atoms. Despite such weak but distinguishable differentiation, similar boron atoms taking the residence in octahedral positions in Pd (see reference 57 in main manuscript) was also demonstrated. Also, Li atomic columns of Li-rich

cathode materials was also recently imaged by the fast-pixel ptychography using the same facilities (Lozano, J. G et al. Nano Lett. 18, 6850–6855, 2018).

Potential issues/questions of this work:

1) The leaching of metal during the reaction and catalytic stability in the repeated reactions:

Our Li-Ag-based catalysts displayed excellent stability in the hydrogenation of dimethyl oxalate (DMO) to methyl glycolate (MG) and/or ethylene glycolate (EG) (Figure 3b in main text) without any attenuation within 200 h. However, the Li-free sample (Ag/SBA-15) displayed relatively inferior durability. Notice that the typical hydrogenation reaction is normally taken place at about 423 to 473 K. Most of metallic particles and promotors (copper, silver, nickel, gold and alkali etc) studied for this reaction are stable for at least several hundred or thousand hours (*Nat. Commun.*, 2018, **9**, 3367; *J. Am. Chem. Soc.*, 2012, **134**, 13922–13925; *J. Catal.*, 2013, **297**, 110–118; *Chem. Commun.*, 2010, **46**, 4348–4350) due their high Tammann temperatures. In short, the leaching/depletion of metals during the reaction over our catalysts does not seem to be a significant issue.

2) Effect of progressive Li addition

The electronic interaction between alkali ions like Li, Na, and K et al., and precious metal (Pd, Pt, Au, and Ru, etc.) has been extensively investigated in heterogeneous catalysis (*Chem. Commun.*, 2017, **53**, 601−604; *Chem. Sci.*, 2021, **12**, 517−532; *Nat. Commun.*, 2020, **11**, 4600). As shown in their results, beneficial modification of electronic change of exposed metal surface could occur between alkali and metal phase. However, excess additive to the metal could be detrimental to catalytic performance due to heavy coverage of active site affecting substrate adsorption/desorption of intermediates or products, thus attenuating overall catalytic performance (*Angew. Chem. Int. Ed.*, 2011, **50**, 2162–2165; *Nat. Commun.*, 2014, **5**, 5787; *Angew. Chem. Int. Ed.*, 2019, **58**, 17335−17341; *J. Am. Chem. Soc.*, 2019, **141**, 19616−19624).

Regarding this point, the Li content was varied over the Ag nanoparticle. As seen, the electronic properties of Ag in $5Ag_1-M_{0.05}$/SBA-15 compared to 5Ag/SBA-15 were studied by XPS (Figure S16). Despite the weak signal of Li in $5Ag_1-M_x$/SBA-15, pronounced spin orbital peaks at around 368.2 eV and 374.2 eV, can be attributed to Ag $3d_{5/2}$ and Ag $3d_{3/2}$ (367.9–361.8 eV and 373.9–374.1 eV), respectively. As seen from Figure R2, the Ag $3d_{3/2}$ peak of $5Ag_1-M_X$/SBA-15 (x ranges from 0.05 to 0.20) gradually shifts to higher BE values indicating that the attenuation in electron density of Ag in comparison with 5Ag/SBA-15.
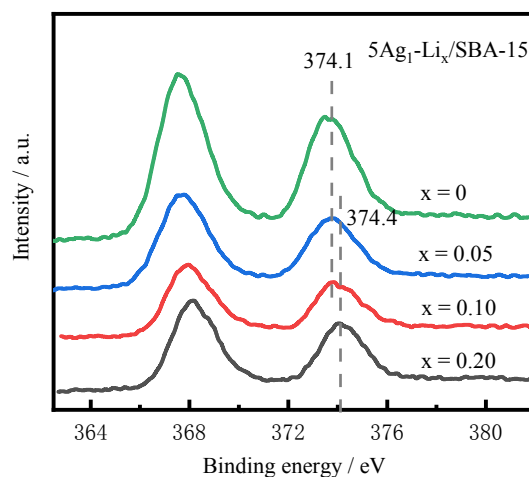
Figure S16. In situ Ag 3d XPS spectra of as-reduced 5Ag/SBA-15 and 5Ag$_1$-M$_x$/SBA-15 catalysts (x referred to the Li content based on the atomic ratio)

3) oxidation state of Ag and its dispersion in the working catalyst.

Regarding the oxidation state of silver, the XPS peaks of Ag 3d$_{5/2}$ and Ag 3d$_{3/2}$ (367.9–361.8 eV and 373.9–374.1 eV) match with the metallic silver after reduction. ^{7}Li MAS was used (see Fig S6). The peak located at 0.71 ppm observed in LiAg/SBA-15 matches with LiNO$_3$ indicating that Li is in cationic form. The EELS study indicated that the elements are well dispersed, see Figure S5.

4) Simple impregnation metal particles tends to deposit the active metal phase near the pore surface. The parameters to control the high dispersion of AG NPS at deep pore cavity include:

Metal nanoparticles deposited near the pore and surface by simple incipient wetness impregnation are preferred due to their simplicity, a small amount of required solvent, availability of metal precursors, and limited waste production. However, as the thermal conditions in drying and calcination steps have a significant influence on the physicochemical features of the final catalyst, to control the properties of metal (oxide) supported NPs with respect to their morphology (shape and size), location, dispersion, and thermal stability are the issues of academic and industrial interest. These properties will ultimately determine the activity, selectivity, and lifetime of the catalyst for applications. Besides the effect of the drying or calcination conditions during IWI preparations, other important factors such as the nature of support and the promoting effect of a second metal must be taken into consideration to control the properties of metal (oxide) supported NPs. Concerning the nature of support, ordered mesoporous silicas such as MCM-41 or SBA-15 are considered ideal hosts for guest NPs due to their large specific surface areas and well-defined pore structures (*Nat. Mater*, 2017, **16**,

132–138; *J. Mater. Chem.*, 2011,**21**, 12529-12541; *Appl. Catal., B*, 2011, **106**, 672–680).

As it is known, TEM represents a powerful tool to study the morphology (shape and size) of nanoparticles as well as to provide local evidence on their distribution on the mesostructured supports. For the samples under study, majority of silver (containing Li promoter) particles is homogenously dispersed accordingly to the TEM images (Figure 2 and Figure S17a) and this suggests that the reduction at high temperature is favorable to prevent the migration of silver particles outside the pore system during the reduction process. Further, irrespective of the calcination temperature, then subsequently reduction, the silver particles appear well dispersed, uniformly distributed and with no visible agglomeration, thus with a high probability to be located inside the channels of mesoporous SBA-15 (images Figure R2*)*. Moreover, these particles present an evenly dispersed polyhedral morphology with particle sizes around 4–5 nm (Figures 1 and 2). However, HRTEM images taken along a direction perpendicular to the pore axis (Figures S17a and b) illustrate the existence of distinct boundaries between particles.

More interestingly, part of the silver nanoparticles is encapsulated by the silica matrix upon high-temperature treatment, as shown in Figure S17b. The synthesis results in an $5Ag_1$-$Li_{0.05}$/SBA-15 material with a considerable loading level of monodispersed silver nanoparticles aligned in the channels.
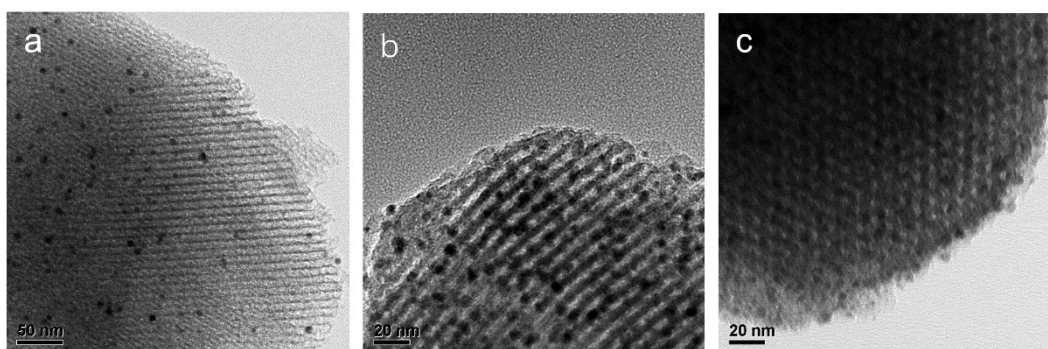

Figure S17. TEM image of as-reduced $5Ag_1$-$Li_{0.05}$/SBA-15 catalyst with different visualizing direction and varied magnified images.

5) Stability of SBA in alkali solution

The influence of alkali ions on the stability of silica-based material like SBA-15 should be carefully

ensured. As known, the alkali solution at high concentration can degrade silica-rich materials, like silicate glasses. It is noted that low content of silver was deliberately set at the level 5 wt% with the Li/Ag atomic ratio of 0.05. We have then conducted and compared the N_2-physisorption, XRD, and HRTEM of fresh and used $5Ag_1$-$Li_{0.05}$/SBA-15 with the unlithiated support. N_2 adsorption-desorption isotherm of the respective catalysts and SBA-15 support indicated the H1-type hysteresis loop (Figure S18a), implying the intact of the porous structure with narrow size distribution after test. In each isotherm, the adsorption inflection at the relative pressure from 0.5 to 0.9 was associated with capillary condensation in the mesopore, and its steepness revealed the uniformity of the mesopore size. These results clearly indicate that the pore structure of SBA-15 support was clearly retained during preparation with the Li solution and after catalytic evaluation. Furthermore, the silver particle with Li retained at a similar size after long-term test. After evaluation for the hydrogenation of DMO, the spent $5Ag_1$-$Li_{0.05}$/SBA-15 catalyst also gave the same diffraction peaks   (JCPDS 00-001-1164) corresponding to characteristic cubic FCC phase Ag (Figure S18b), wherein the lattice distance and particle size were similar to the reduced $5Ag_1$-$Li_{0.05}$/SBA-15 sample. We therefore conclude that the Li solution at the concentration we employed does not seem to affect the structure and morphology of the catalyst. We have included the above comment in the revised supporting information for readers to appreciate the catalyst stability upon lithium inclusion.
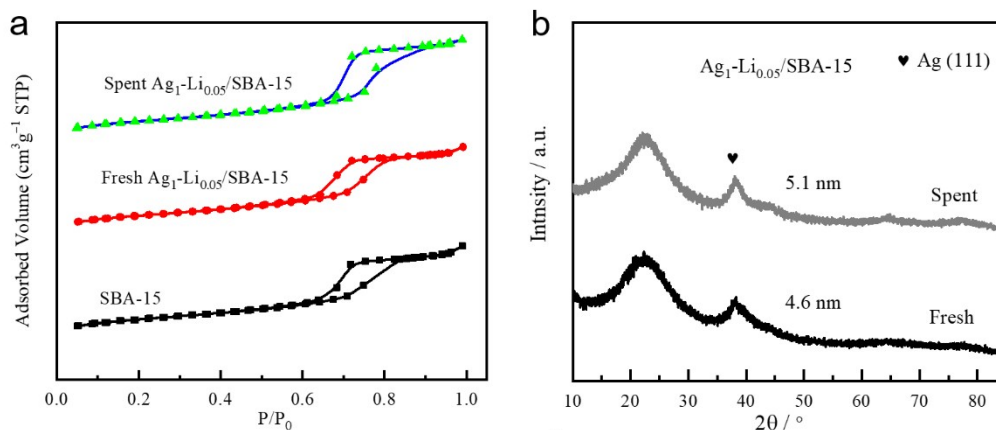
Figure S18. Characterization of fresh and spent SBA-15 based catalysts and SBA-15 support by N_2 adsorption isotherms (a), XRD patterns of fresh and spent lithium promoted silver nanoparticles on SBA-15 support (b)

6) Previous backgrounds of the mechanism of the reaction

As known, semi hydrogenation of DMO to MG (first stage hydrogenation) without over hydrogenation of DMO to EG/EtOH (second stage hydrogenation) requires careful tuning of the catalyst surface affinity for optimal absorption of substrate/intermediate. Importantly, the second hydrogenation step is two orders of magnitude larger in adsorption energy for partial hydrogenated intermediate than that of the first step of DMO (*J. Am. Chem. Soc.*, 2012, 134, 13922−13925; *J. Catal.*, 2013, 297, 110−118; *Chem. Commun.*, 2010, 46, 4348−4350). Therefore, for tandem hydrogenation reactions, the development of an efficient catalyst to control and regulate the target products is still a great challenge for both academia and industry. Using the reduced electron density on Ag surface via addition of alkali ions appears to be advantageous for the hydrogenation of DMO to MG since the rate-determining step is on the excessive adsorption of intermediate rather than DMO. (Catal. Sci. Technol., 2019,9, 5763-5773; *Sci. Adv.* 2018, 4, eaau3275; *Ind. Eng. Chem. Res.* 2015, 54, 1243−1250). Thus, by weakening the adsorption of intermediate(s), higher selectivity of MG can be optimised with the tuning of the conditions for the maximum space time yield.

Reference

1. Bondi, A. van der Waals Volumes and Radii. *J. Phys. Chem.* **68**, 441−451 (1964).

2. N.N. GREENWOOD；A. EARNSHAW. *Chemistry of the Elements*. (Elsevier, 1997). doi:10.1016/C2009-0-30414-6

3. Shannon, R. D. Revised effective ionic radii and systematic studies of interatomic distances in halides and chalcogenides. *Acta Crystallogr. Sect. A* **32**, 751−767 (1976).

4. Mantina, M., Chamberlin, A. C., Valero, R., Cramer, C. J. & Truhlar, D. G. Consistent van der Waals Radii for the Whole Main Group. *J. Phys. Chem. A* **113**, 5806−5812 (2009).

5. Silver|EELS.info. Available at: https://eels.info/atlas/silver. (Accessed: 20th July 2020)

6.   Ahn, C. C.; Krivanek, O. L. D. M. M. *EELS atlas: a reference collection of electron energy loss spectra covering all stable elements*. (Gatan Inc, 1983).

7.   Hayes, S. E., Guidotti, R. A., Even, W. R., Hughes, P. J. & Eckert, H. 7 Li Solid-State Nuclear Magnetic Resonance as a Probe of Lithium Species in Microporous Carbon Anodes. J. Phys. Chem. A 107, 3866–3876 (2003).

8.   Dupre, N., Cuisinier, M. & Guyomard, D. Electrode/Electrolyte Interface Studies in Lithium Batteries Using NMR. Interface Mag. 20, 61–67 (2011)

9.   Chupas, P. J., Qiu, X., Hanson, J. C., Lee, P. L., Grey, C. P., Billinge, S. J. L. J. Appl. Crystallogr., 2003, 36, 1342–1347.

10.   Cowley, J. M. & Moodie, A. F. The scattering of electrons by atoms and crystals. I. A new theoretical approach. *Acta Crystallogr.* **10**, 609–619 (1957).

11.   Goodman, P. & Moodie, A. F. Numerical evaluations of N -beam wave functions in electron scattering by the multi-slice method. *Acta Crystallogr. Sect. A* **30**, 280–290 (1974).

12.   Lobato, I. & Van Dyck, D. MULTEM: A new multislice program to perform accurate and fast electron diffraction and imaging simulations using Graphics Processing Units with CUDA. *Ultramicroscopy* **156**, 9–17 (2015).

13.   Loane, R. F., Xu, P. & Silcox, J. Thermal vibrations in convergent-beam electron diffraction. *Acta Crystallogr. Sect. A Found. Crystallogr.* **47**, 267–278 (1991).

14.   A. Muller, D., Edwards, B., J. Kirkland, E. & Silcox, J. Simulation of thermal diffuse scattering including a detailed phonon dispersion curve. *Ultramicroscopy* **86**, 371–380 (2001).

15.   Peng, L.-M., Ren, G., Dudarev, S. L. & Whelan, M. J. Debye–Waller Factors and Absorptive Scattering Factors of Elemental Crystals. *Acta Crystallogr. Sect. A Found. Crystallogr.* **52**, 456–470 (1996).

16.   Yang, H. *et al.* Electron ptychographic phase imaging of light elements in crystalline materials using Wigner distribution deconvolution. *Ultramicroscopy* **180**, 173–179 (2017).

17. Hÿtch, M. J. & Stobbs, W. M. Quantitative comparison of high resolution TEM images with image simulations. *Ultramicroscopy* **53**, 191–203 (1994).